Computations of Supersonic Flows Over a Body at High Angles of Attack

O. Baysal* and K. Fouladi†
Old Dominion University, Norfolk, Virginia
and
D. S. Miller‡
NASA Langley Research Center, Hampton, Virginia

Three-dimensional supersonic flows over a blunt-nose-cylinder at 20, 32, and 44 deg angles of attack were computed. Length-to-diameter ratio of the cylinder used for the computations was 6.67 with a base diameter of 3 in. The flowfield was dominated by large-scale, multiple vortices generated by the crossflow separation. The mass averaged Navier-Stokes equations were solved by an approximately factored, upwind-biased, implicit, finite volume scheme. The Reynolds shear stress terms were modeled algebraically with modifications to correct the turbulent length and velocity scales in separated regions. The initializations of the flows were enhanced by a mesh sequencing strategy applied to the diagonalized form of the discretized equations. The convergence to steady-state was accelerated by a multigrid algorithm that used the block inversions for the discretized equations. Calculations were compared successfully with experimental results.

Nomenclature

C_N = normal force coefficient
c_p = pressure coefficient
D,L = cylinder diameter and length
e = energy per unit volume
M = freestream Mach number
p = pressure
Re = freestream Reynolds number
T_T = freestream total temperature
u,v,w = Cartesian velocity components
x,y,z = Cartesian coordinates
α = angle of attack
μ = coefficient of molecular viscosity
ρ = density

Introduction

THE viscous effects on the supersonic aerodynamics of stores or missiles had been ignored in calculations until recently because of the difficulties involved. Currently, there exist a few reports of viscous calculations.[1-4] The existence of shock waves in the vicinity of the forebody, separated boundary layers on the leeside with development of symmetric or asymmetric vortices, and the formation of wake-like leeside flow at very large angles of attack, contribute to the complications encountered. The accuracy of the solutions depends on factors such as the necessity of highly stretched grids to resolve the extensive regions of separation.

As indicated in Ref. 5, the flow patterns that a body-of-revolution experiences as it is pitched from 0–90 deg angle of attack fall into four categories, which reflect the diminishing influence of the axial flow (Fig. 1). At moderate angles of attack ($\alpha \simeq 10$ deg), the crossflow about the body begins to separate over the leeside generating symmetrical, counter-rotating vortices on the leeside.[4] At large incidences and depending on a number of other factors, the vortices over the leeside may become asymmetric, and consequently, the body experiences a large side force and a yawing moment. Longer bodies develop multiple asymmetric vortex pairs resembling a Kármán vortex street. One of the methods of increasing the lateral stability is to increase the bluntness of the nose, which has the effect of delaying the onset of asymmetrical vortex shedding. Besides the angle of attack, factors determining the structure of the flowfield include the compressibility (Mach number), the Reynolds number, and the shape of the body (forebody, afterbody, cross section). Critical Reynolds numbers, which may be loosely defined to mark the boundaries between laminar, transitional, and turbulent flow conditions, are also affected by the angle of attack. Lamont[6] has shown that the critical Reynolds number boundary between transitional and turbulent separation is a strong function of the angle of attack, whereas the laminar-transitional separation boundary varies much less with the incidence.

The purpose of the present Navier-Stokes calculations was to provide solutions for supersonic flows over a blunt-nose-cylinder at high angles of attack, which compare favorably with experiments, and to show the effect of turbulence on the separation characteristics. Three laminar flow cases and one turbulent flow case were numerically simulated with special attention given to numerical and computational efficiencies.

Mathematical Formulation

The governing equations are the thin-layer approximations to the Reynolds-averaged Navier-Stokes equations written in conservative form and generalized curvilinear coordinates ξ,η,ζ;

$$\partial_t Q + \partial_\xi F + \partial_\eta G + \partial_\zeta (H - H_v) = 0 \tag{1}$$

The validity of the thin-layer viscous model for flows with massive crossflow separation was assessed in Ref. 1, by comparing the results obtained with and without the circumferential viscous terms and viscous cross-derivative terms. It was found that the inclusion of these terms caused only slight

Presented as Paper 88-0485 at the AIAA 26th Aerospace Sciences Meeting, Reno, NV, Jan. 11-14, 1988; received Jan. 15, 1988; revision received May 18, 1988.

*Associate Professor, Mechanical Engineering and Mechanics Department. Member AIAA.
†Graduate Research Assistant, Mechanical Engineering and Mechanics Department.
‡Head, Supersonic/Hypersonic Aerodynamics Branch, HSAD. Member AIAA.

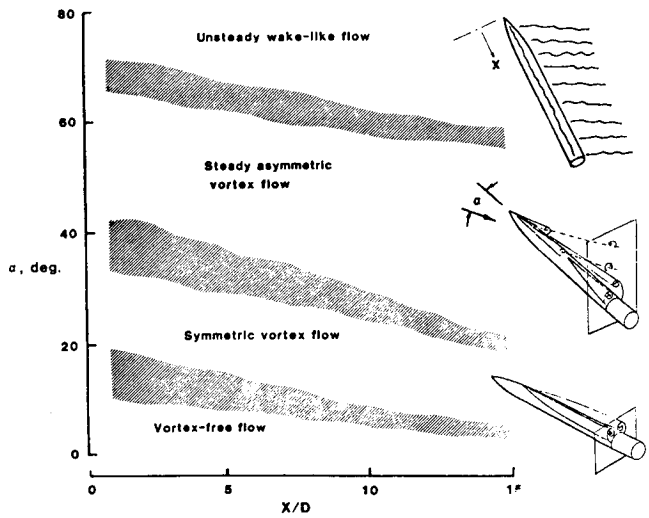

Fig. 1 Approximate flow regimes for bodies of revolution from Ref. 5.

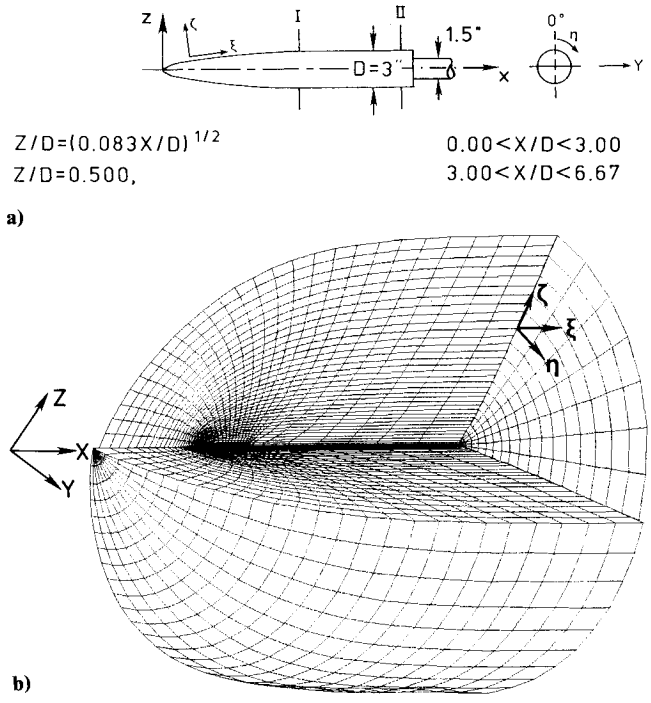

Fig. 2 a) The schematic of the blunt-nose-cylinder; and b) a representative grid section.

changes in the computed solutions (less than 0.5%), but increased the computation time by 11%. The definition of the Cartesian and generalized coordinates, which are used to map the body surface into the $\zeta = 0$ plane, are shown in Fig. 2. The conserved variables of vector $\boldsymbol{Q}$

$$Q = [\rho,\ \rho u,\ \rho v,\ \rho w,\ e]^T/J \tag{2}$$

were normalized with the cylinder diameter, and the free-stream values of the density, the local speed of sound and the molecular viscosity. The flux vectors $\boldsymbol{F}$, $\boldsymbol{G}$, $\boldsymbol{H}$, and $\boldsymbol{H}_v$ are

$$\boldsymbol{F} = (1/J)[\rho U,\ \rho Uu + \xi_x p,\ \rho Uv + \xi_y p,\ \rho Uw + \xi_z p,\ (e+p)U]^T \tag{3}$$

$$\boldsymbol{G} = (1/J)[\rho V,\ \rho Vu + \eta_x p,\ \rho Vv + \eta_y p,\ \rho Vw + \eta_z p,\ (e+p)V]^T \tag{4}$$

$$\boldsymbol{H} = (1/J)[\rho W,\ \rho Wu + \zeta_x p,\ \rho Wv + \zeta_y p,\ \rho Ww + \zeta_z p,\ (e+p)W]^T \tag{5}$$

$$\boldsymbol{H}_v = (1/J)[0,\ \zeta_x \tau_{xx} + \zeta_y \tau_{xy} + \zeta_z \tau_{xz},\ \zeta_x \tau_{xy} + \zeta_y \tau_{yy} + \zeta_z \tau_{yz},\ \zeta_x \tau_{xz} + \zeta_y \tau_{yz} + \zeta_z \tau_{zz},\ \zeta_x b_x + \zeta_y b_y + \zeta_z b_z]^T \tag{6}$$

where J is the transformation Jacobian

$$J = \frac{\partial(\xi,\eta,\zeta)}{\partial(x,y,z)} \tag{7}$$

and U, V, and W are the contravariant velocities

$$U = \xi_x u + \xi_y v + \xi_z w \tag{8}$$

$$V = \eta_x u + \eta_y v + \eta_z w \tag{9}$$

$$W = \zeta_x u + \zeta_y v + \zeta_z w \tag{10}$$

The ratio of a metric derivative to the transformation Jacobian for a given cell, for example ξ_x/J, was taken to be the appropriate projected area of a cell face, and the reciprocal of the Jacobian was taken to be the cell volume. The magnitude of the directed area and one of its direction cosines at a cell interface were computed, for example at a fixed ξ-location and in the x-direction, as ($|\text{grad}\ \xi/J|$) and ($-\xi_x/|\text{grad}\ \xi|$), respectively. This approach ensured the geometric conservation law compatible with the finite volume formulation used. The shear stress τ and the heat flux $\dot{q}$ terms written in shorthand tensor notation are

$$\tau_{x_i x_j} = \frac{M}{Re_D}\left[\mu\left(\frac{\partial u_i}{\partial x_j} + \frac{\partial u_j}{\partial x_i}\right) + \lambda\frac{\partial u_k}{\partial x_k}\delta_{ij}\right] \tag{11}$$

$$b_{x_i} = u_j\,\tau_{x_i x_j} - \dot{q}_{x_i} \tag{12}$$

$$\dot{q}_{x_i} = \left(\frac{-M}{Re_D Pr(\gamma-1)}\right)\frac{\partial c^2}{\partial x_i} \tag{13}$$

where Pr represents the laminar Prandtl number, γ is the ratio of specific heats, and δ is the Kronecker delta. The ideal gas law was used for closure, and the Sutherland law was used to relate μ to the temperature. The bulk viscosity λ was related to μ through the Stokes law.

The turbulent Reynolds stress resulting from mass averaging was assumed proportional to the laminar stress tensor with the coefficient of proportionality defined as the eddy viscosity μ_t. Similarly, the turbulent Reynolds heat flux was assumed to be proportional to the laminar heat flux with the coefficient of proportionality defined as $(\gamma R\,\mu_t)/[Pr_t(\gamma-1)]$, where Pr_t is the turbulent Prandtl number and R is the specific gas constant. The local values of the eddy viscosity were computed using the Baldwin-Lomax turbulence model.[7] Then, Eqs. 11 and 13 were modified with

$$(\mu + \mu_t),\ [(\mu/Pr) + (\mu_t/Pr_t)] \tag{14}$$

Although the genesis of algebraic eddy viscosity turbulence models, which depend only on the local flow profiles, is based on two-dimensional boundary layer flows, their use for complex vortical flows having regions of massive crossflow separation can be justified.[1] The vortical leeside flow can be viewed

as if it consists of multiple boundary layers. The vortex structure is governed primarily by the convection of vorticity generated within these boundary layers at the body surface. Since the primary direction of these boundary layers is streamwise, they should all be turbulent under the conditions where the windside flow is turbulent. However, the model had to be modified in order to determine the proper length and velocity scales for the regions with massive crossflow separation.[1,2] The wake function and the velocity scale, which were used in determining the outer μ_t value, showed multiple peaks in these regions. In addition to a local peak in the attached boundary layer, a larger peak was caused by the overlying vortex structure. The choice of this larger peak would yield an erroneous μ_t value. Also, these peaks were almost merged in regions where an onset of separation or a reattachment existed. Proper search methods had to be devised to avoid such exaggerated outer μ_t values.

Solution Algorithm

The solution was achieved using the implicit, finite-volume, upwind algorithm described in Refs. 8–11. Roe flux-difference splitting was used to construct the upwind differences for the convective and pressure terms. A consequence of this type of upwinding is when an eigenvalue of a flux Jacobian vanishes, the corresponding eigenvalue of the dissipation matrix also vanishes. This leads to a crisp resolution of discontinuities, such as shocks. Spatial derivatives were written conservatively as flux balances across a cell. The Roe-averaged ($\hat{}$) cell interface values of fluxes were evaluated after a state variable Q interpolation where the primitive variables ρ, u, v, w, and p were used. This method assumed locally one-dimensional model of wave interactions perpendicular to these interfaces. The diffusion terms were centrally differenced. The accuracy of this scheme was second-order spatially and first-order temporally. Spatial approximate factorization and Euler backward time integration resulted in the solution through 5×5 block-tridiagonal matrix inversions in three directions. The delta form of Eq. (1) obtained in this manner is given here

$$\left[\frac{I}{J\Delta t} + \delta_\xi(\partial_Q \hat{F})\right] \times \left[\frac{I}{J\Delta t} + \delta_\eta(\partial_Q \hat{G})\right] \times \left[\frac{I}{J\Delta t} + \delta_\zeta\left(\partial_Q \hat{H} - \frac{M}{Re}\partial_Q \hat{H}_v\right)\right] \times \Delta Q = -\mathrm{Res}(Q^n) \quad (15)$$

$\mathrm{Res}(Q^n)$ is the discretized representation of the spatial derivative terms in Eq. (1) evaluated at time level n. In Eq. (15), δ denotes an upwind difference and Δ denotes a finite increment.

To accelerate the convergence to a steady state, a sequence of grids were formed by deleting every other mesh line on the next finest grid. The finest grid was called the first-level grid, and the coarsest grid used herein was the fourth-level grid. The computation was stated with the initialization of the fourth-level grid with freestream values of the conserved variables. When satisfactory convergence was accomplished (based on the time histories of the lift coefficient rather than the logarithm residual, due to relatively poor damping characteristics of centrally differenced viscous calculations on highly stretched grids), the solution was carried to the third-level grid. This process was repeated until the solution was gradually carried to the finest grid (first-level). This "mesh sequencing" strategy reduced the amount of computational time required to get past the initial transients.

Another computational time-saving measure used for the initialization of the flowfield was to employ the diagonal form of the spatial factors of Eq. (15). For example,

$$\left[\frac{I}{J\Delta t} + \delta_\eta(\partial_Q \hat{G})\right] \cong T\left[\frac{I}{J\Delta t} + \delta_\eta^- \Lambda^+ + \delta_\eta^+ \Lambda^-\right] T^{-1} \quad (16)$$

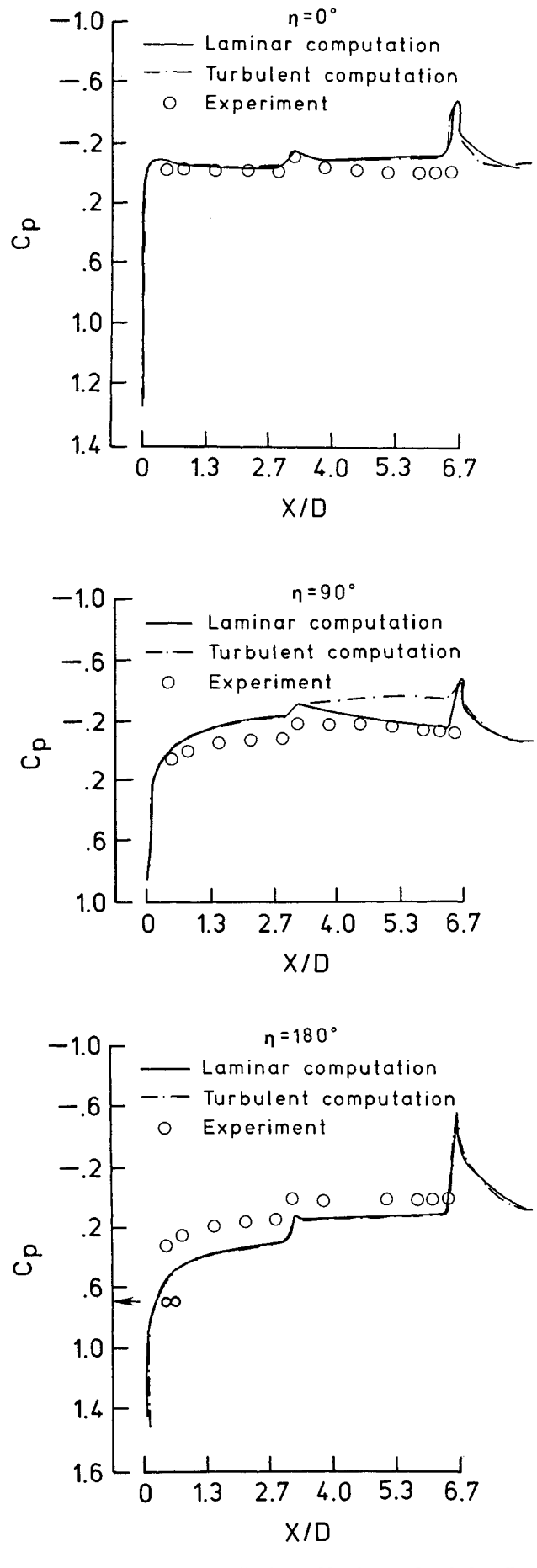

Fig. 3 Longitudinal C_p distributions of laminar and turbulent flows for $\alpha = 20$ deg in comparison with their experimental[12] values.

where $\Lambda^{\pm} = (\Lambda \pm |\Lambda|)/2$ are the diagonal eigenvalue matrices and $T^{\pm}$ are the diagonalization matrices. Due to the repeated eigenvalues of Λ, only scalar diagonal inversions rather than block inversions were used in each direction.

After completing the initialization by mesh sequencing, the diagonal inversions [Eq. (16)] were turned off, and 5×5 block inversions for the solution of Eq. (15) were used during the multigrid cycles. The high-frequency error component on a given grid level was resolved on the same level by the solution algorithm explained above. The remaining low-frequency error component appeared as a high-frequency error on a coarser level grid, which in turn was reduced by the same solution algorithm that was capable of resolving high-frequency errors. A fixed cycling strategy was adopted, where a predetermined number of iterations were performed at each grid level. The calculations were passed from a finer grid to a coarser grid through volume-weighted restrictions. When the coarsest level was reached, computed ΔQ values of each level were prolonged to the second level through a series of bilinear interpolations. Then this sequence was repeated one more time to complete one cycle (W-cycle). This procedure helped the improvement of the overall robustness of the computations.

The C-O type grids used in this study were generated by first solving the two-dimensional Poisson's equations for half of the symmetry plane of the cylinder (XZ-plane), then rotating this grid about the axis of the cylinder (Fig. 2). The minimum normal spacings were on the order of $10^{-4} \times D$. Due to assumed symmetry of flows for $\alpha = 20$ deg cases, the grid used was around half of the body ($\eta = 0$–180 deg). The $\alpha = 32$ deg and $\alpha = 44$ deg cases were computed on the grid about the full body ($\eta = 0$–360 deg) and consisted of 374,000 cells.

No slip and impermeability wall boundary conditions, zero-normal-gradient for wall pressure, and isothermal-wall conditions were imposed. First-order extrapolations of the conserved variables were used along the downstream boundary. The outer boundary conditions were specified after a flow

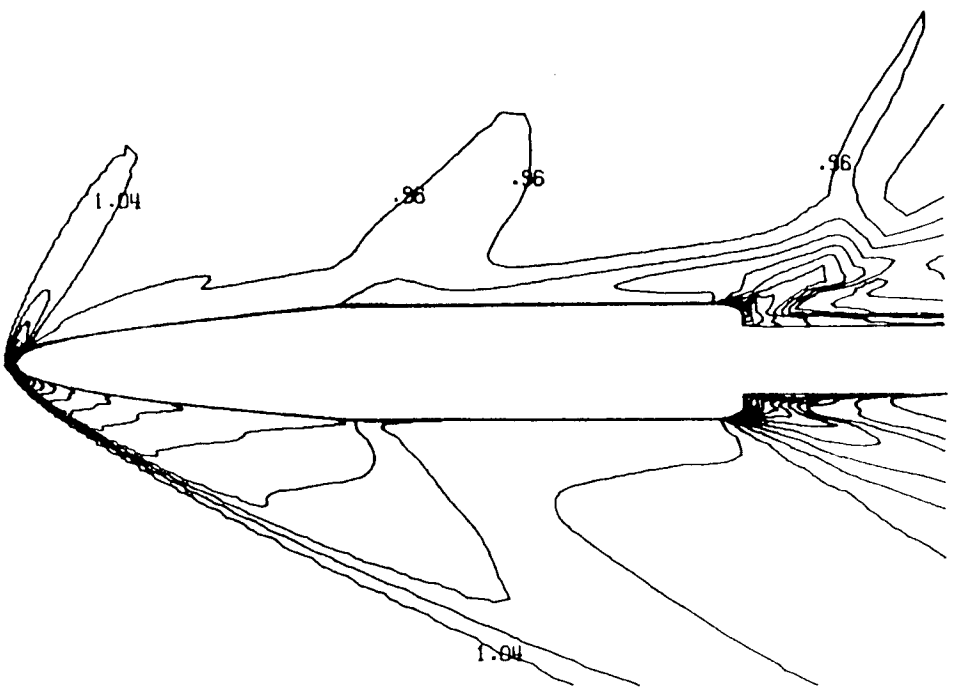

a) DENSITY CONTOURS MIN VALUE= .1051 MAX= 2.4470

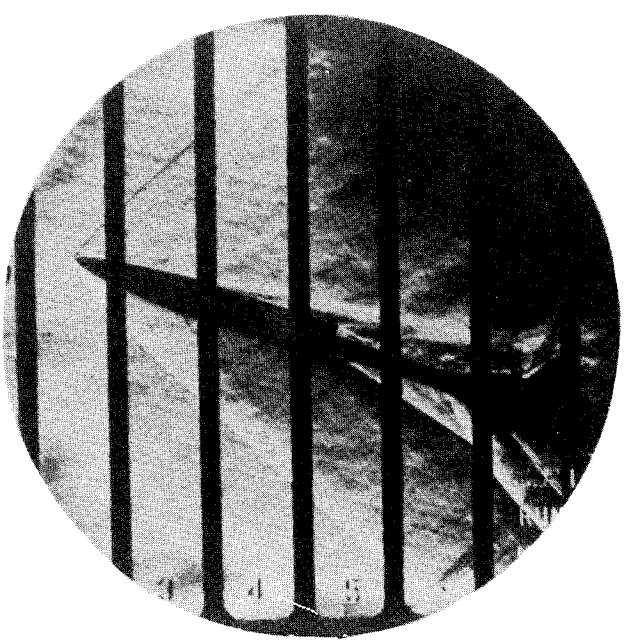

b)

Fig. 4 a) Normalized density contours; and b) Schlieren photograph[12] of the symmetry plane for $\alpha = 20$ deg.

direction check. When the sign of the dot product of velocity vector and cell area vector was negative (inflow), property values were set equal to their freestream values. When this product was positive (outflow), first-degree extrapolation from the computation zone was employed. The cut-plane of C-mesh was treated by averaging the property values from both sides of the cut. The velocity component normal to the symmetry-plane was set equal to zero for the half-body computations.

Since only steady-state solutions were sought, the time advancement was done by setting the Courant number constant, rather than the time step, for all the cells (local time stepping). The computer program was written in explicit vectorization using the proper syntax, which allows single-instruction-multiple-data (SIMD) processing.[10] The computational times required for the convergence of 20 and 32 deg angle of attack cases were approximately 35 and 55 min, respectively, on NASA Langley VPS-32 (Cyber-205) vector processor using 64-bit arithmetic. The computational rates (CPU time per iteration per cell) were around 83 μs when 5×5 block inversions were performed and about 30 μs when diagonal inversions were performed. The turbulent $\alpha = 20$ deg case required 5 more minutes of CPU time than the laminar $\alpha = 20$ deg case. The case of $\alpha = 44$ deg required about 2 hrs of CPU time for convergence. The stability bounds for the diagonal algorithm appeared to have been reached for this case. Thence 5×5

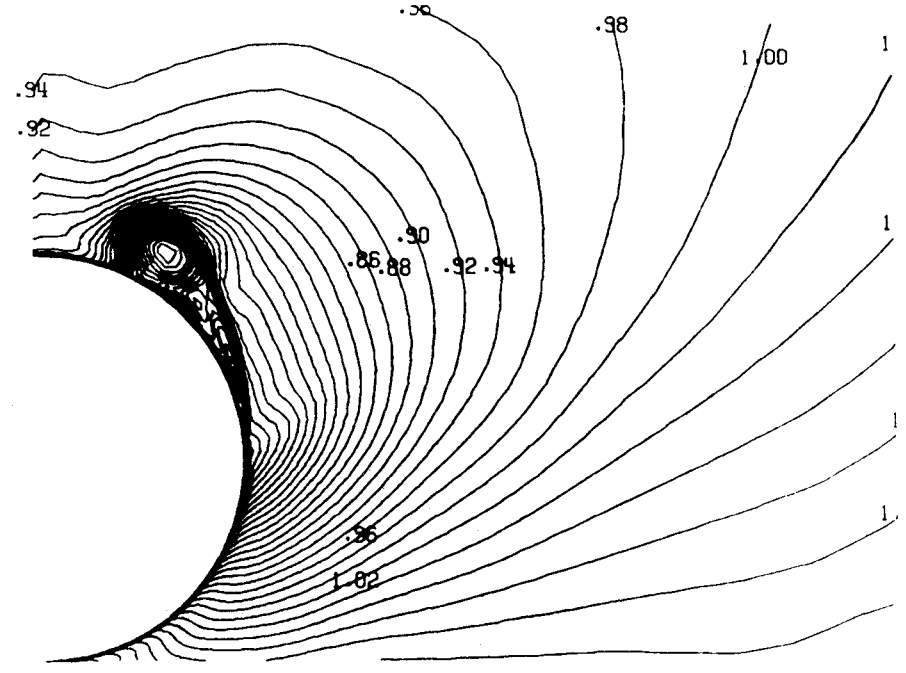

a) DENSITY CONTOURS MIN VALUE= .2839 MAX= 1.2658

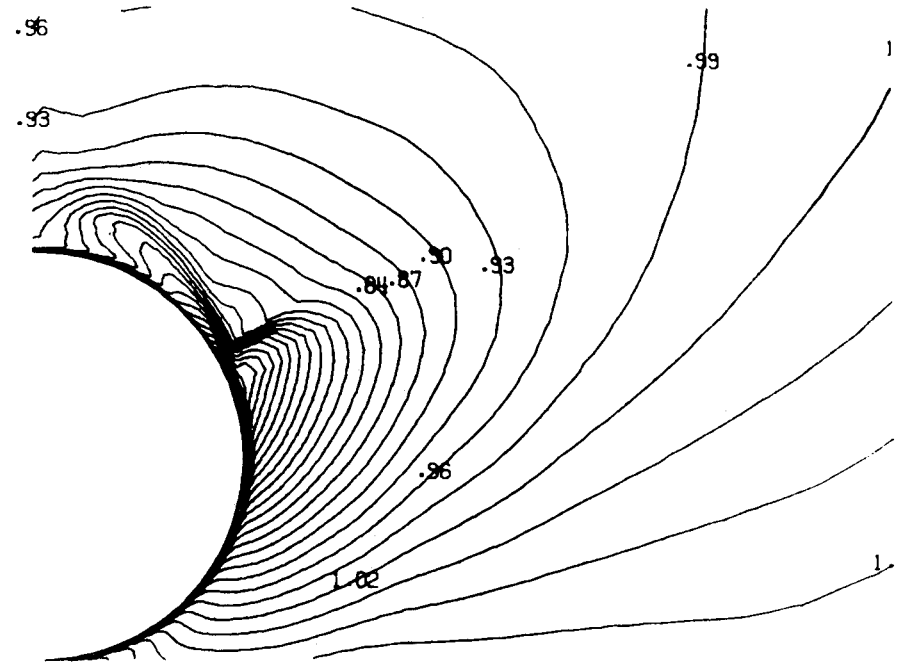

b) DENSITY CONTOURS MIN VALUE= .2042 MAX= 1.2698

Fig. 5 Normalized crossflow density contours for a) laminar flow and b) turbulent flow at Station I for $\alpha = 20$ deg.

block inversions for the full equation [Eq. (15)] had to be used even for the initialization. In an attempt to demonstrate the total efficiency, the number of equivalent-single-grid-iterations (NESGI) was loosely defined as the ratio of total CPU time to complete a case using all the efficiency measures explained above, to the CPU time for one iteration on the finest grid using only block inversions. The NESGI values for laminar $\alpha = 20$ and 44 deg cases were approximately 70 and 250, respectively.

Results and Discussion

The blunt-nose-cylinder chosen to demonstrate the objectives of the study was adopted from Ref. 12 (Fig. 2). The freestream conditions chosen for the illustrative computational test cases were as follows:

$M = 1.6$, $Re/\text{ft} = 2 \times 10^6$, $Re_D = 5 \times 10^5$

$T_T = 585$ deg R, $L/D = 6.67$, $D = 3$ in.

$\alpha = 20$ deg laminar flow simulation on half-body

$\alpha = 20$ deg turbulent flow simulation on half-body

$\alpha = 32$ deg laminar flow simulation on full-body

$\alpha = 44$ deg laminar flow simulation on full-body

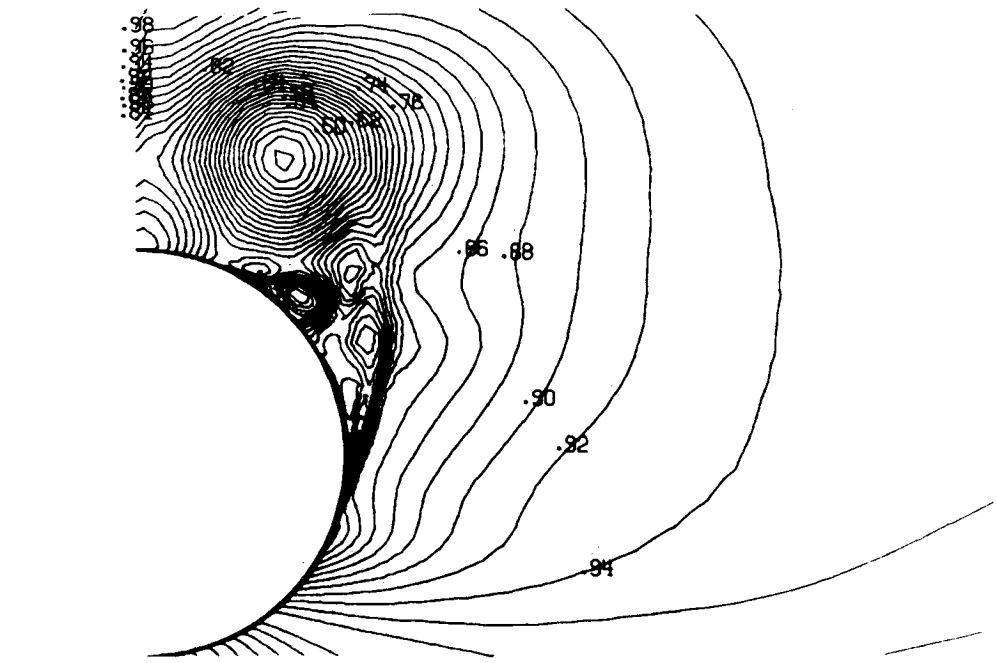

a) DENSITY CONTOURS MIN VALUE= .3767 MAX= 1.1674

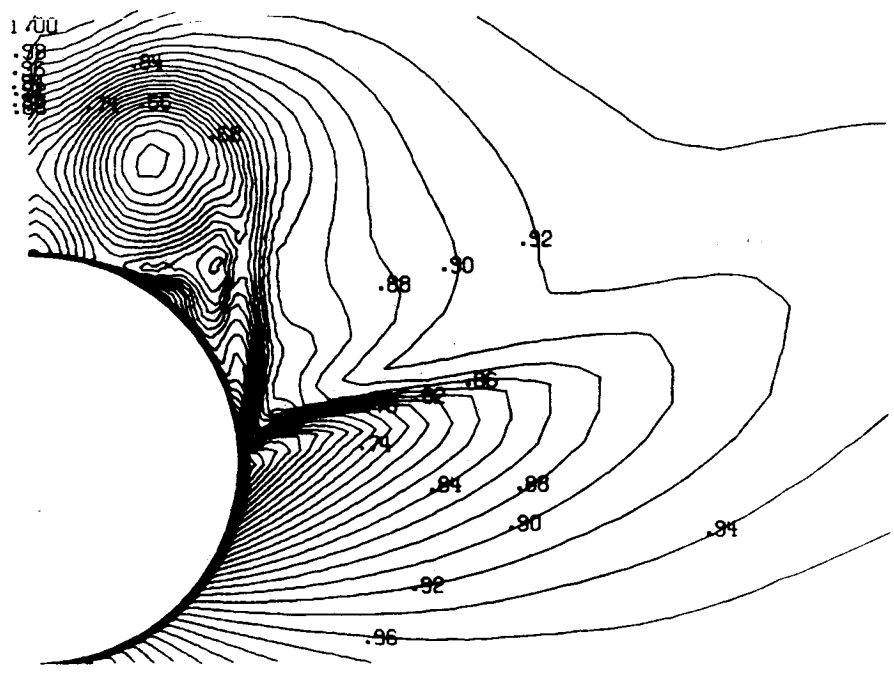

b) DENSITY CONTOURS MIN VALUE= .2636 MAX= 1.1699

Fig. 6 Normalized crossflow density contours at Station II for $\alpha = 20$ deg: a) laminar flow; and b) turbulent flow.

Laminar Flow at $\alpha = 20$ Deg

Longitudinal distributions of computed and experimentally measured[12] values of surface pressure coefficients at fixed circumferential stations ($\eta = 0$, 90, and 180 deg) are presented in Fig. 3. The discrepancies between the computed and experimental C_p values are largest for $\eta = 180$ deg. This could be attributed to the circumferential clustering of the grid toward the leeside. The normal force coefficient at this angle of attack was computed to be 2.03, which compared reasonably with its experimentally measured value, 1.92. The base was used as the reference area in computing force coefficients. Figure 4 shows the computed density contours of the symmetry plane in qualitative comparison with its Schlieren photograph obtained in the Unitary Plan Wind Tunnel of NASA Langley Research Center.[12]

Two axial stations were chosen to analyze the crossflow. Stations I and II (Fig. 2a) were located immediately after the forebody-cylinder junction ($X/D = 3.17$) and upstream of the base ($X/D = 6.17$), respectively. A comparison of the density contours at these stations (Figs. 5a and 6a) shows that the strength of the primary vortices grows with increased distance downstream from the nose. Subsequent to the primary reattachment point ($\eta \simeq 0$ deg), the flow is toward the windside of the body. The circumferential skin friction coefficient (C_f) distribution at Station II (Fig. 7) indicates that the primary separation occurs around $\eta = 106$ deg. This induced flow leaves the surface at a secondary separation point through a weak crossflow shock around $\eta = 27$ deg, with the fluid rolling up to form a secondary vortex and reattaching around $\eta = 81$ deg. Crossflow separation may also be indicated by the convergence (Ref. 4) of the skin friction patterns (limiting streamlines). However, the exact circumferential location of the onset of separation may not be coincident with the convergence. The limiting streamlines of this case (Fig. 8a) show that the separation lines on the body move downward from the leeside to the windside with increased distance downstream from the nose.

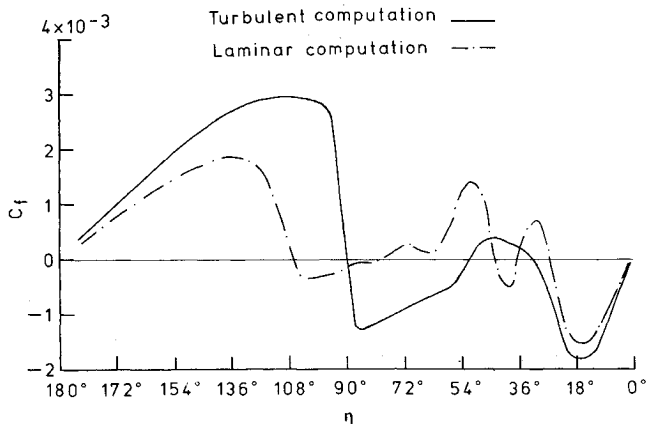

Fig. 7 Circumferential skin friction distributions at Station II for $\alpha = 20$ deg.

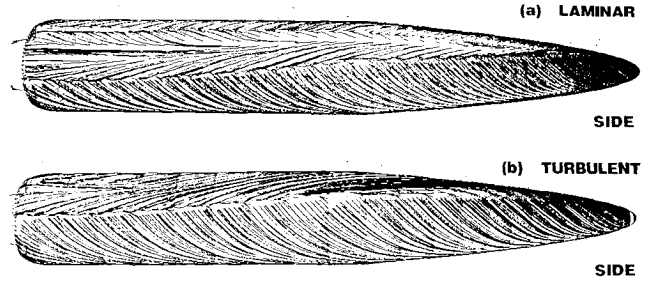

Fig. 8 Side views of skin friction patterns for $\alpha = 20$ deg: a) laminar flow; and b) turbulent flow.

Turbulent Flow at $\alpha = 20$ Deg

The question arose at this point whether the flow under the conditions given above for this case was laminar, transitional, or fully turbulent. Lamont[6] indicated that the flow at $\alpha = 20$ deg and $Re_D = 5 \times 10^5$ about an ogive cylinder would be on the verge of becoming fully turbulent. Considering the fact that the cylinder in this study had a blunt nose, and the flow on the surface of the body was strongly influenced by the upstream conditions, an attempt to answer this question is not made herein. However, both laminar and fully turbulent flow

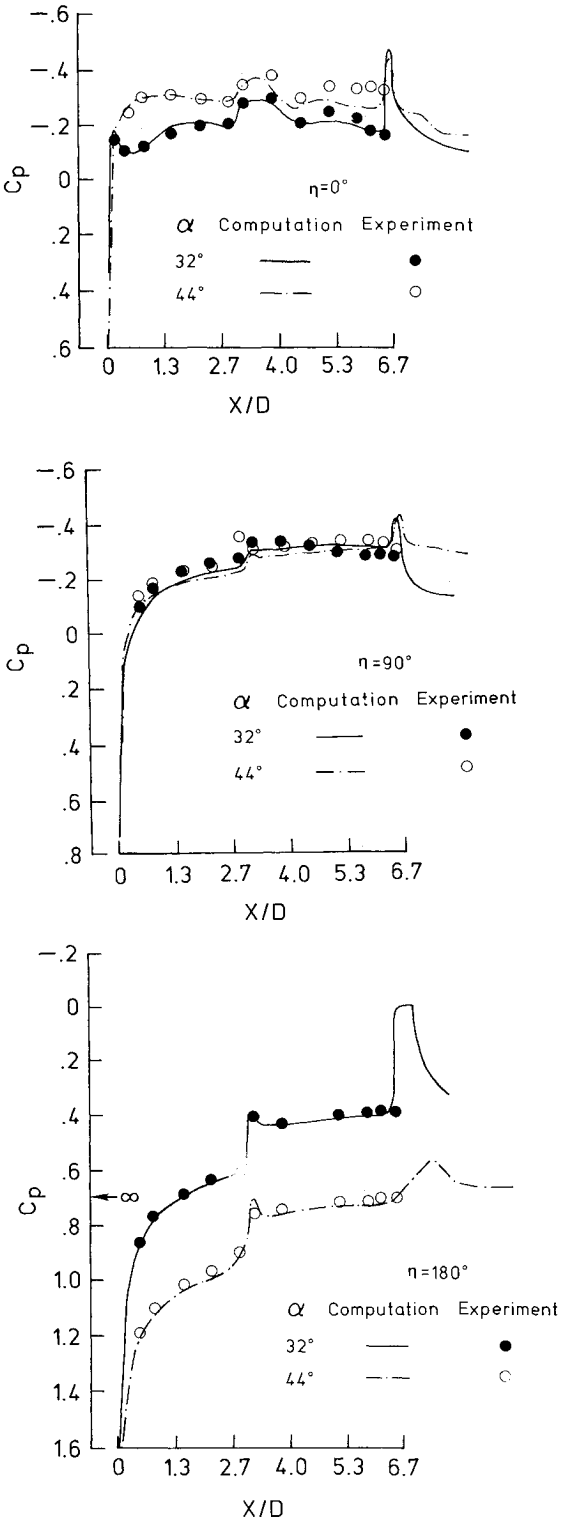

Fig. 9 Longitudinal C_p distributions of $\alpha = 32$ deg and $\alpha = 44$ deg flows in comparison with their experimental[12] values.

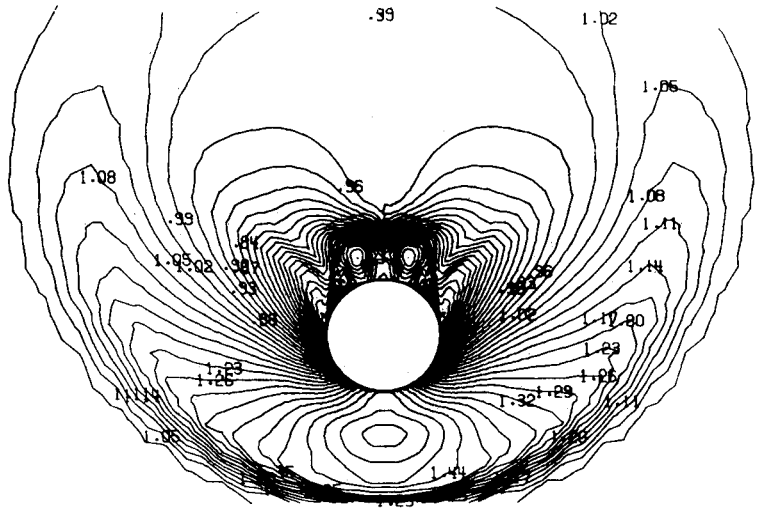

a)

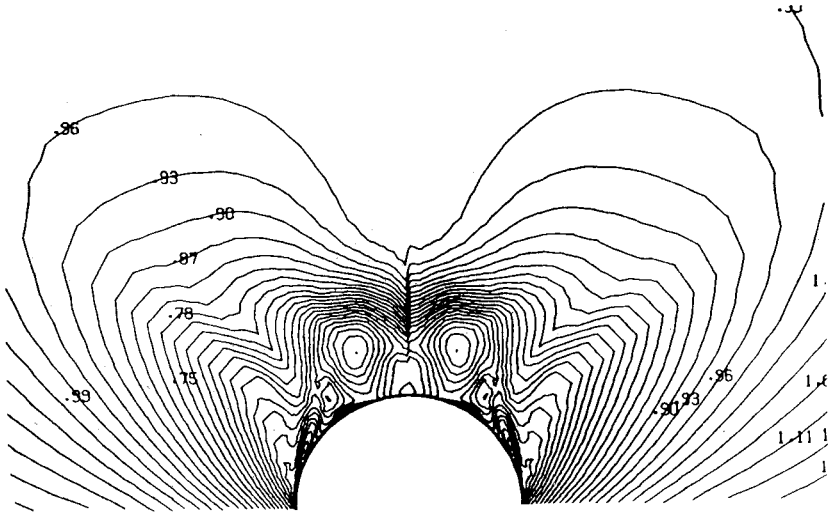

b)

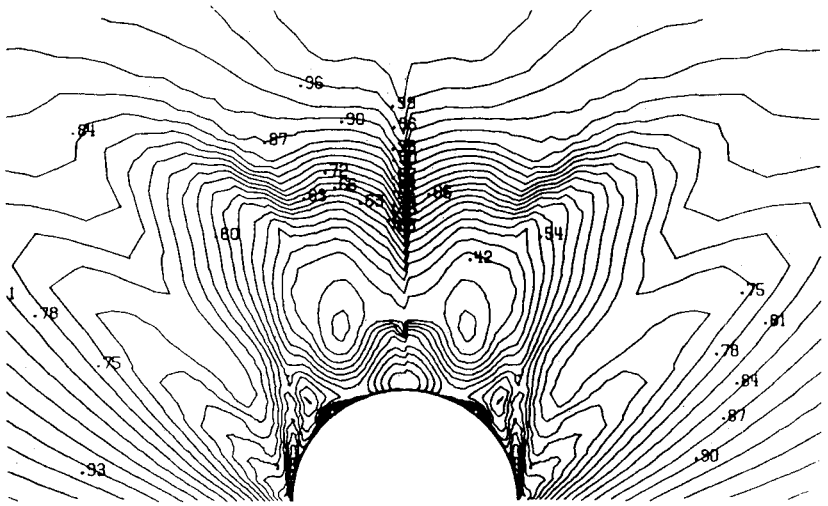

c)

Fig. 10 Normalized crossflow density contours for $\alpha = 32$ deg: a) Station I; b) enlarged view of leeside flow at Station I; and c) Station II.

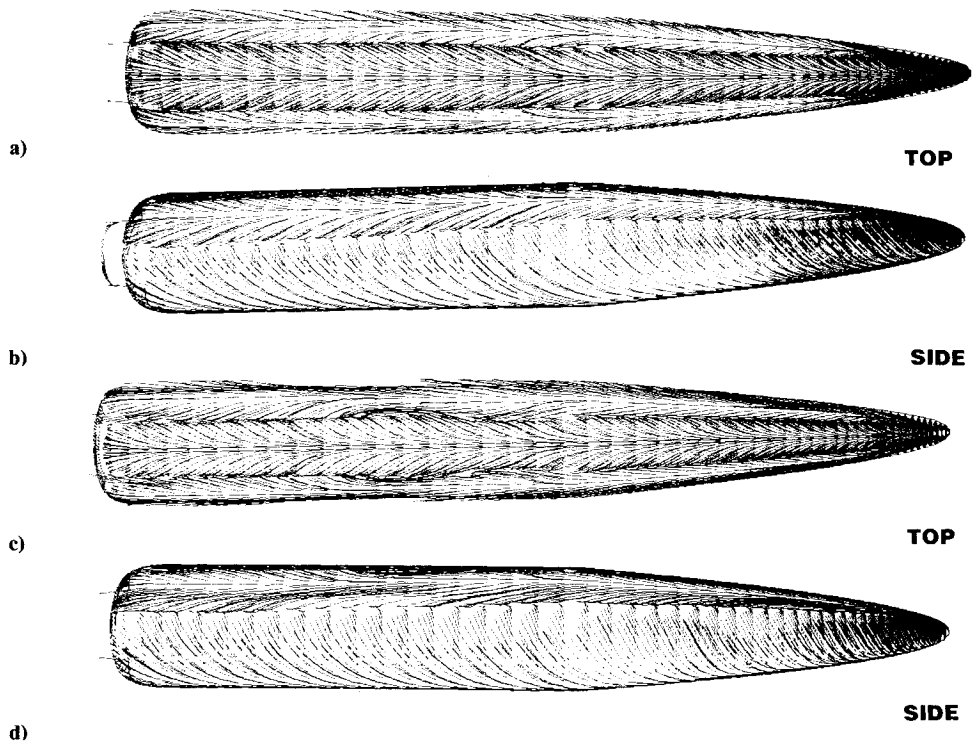

Fig. 11 Skin friction patterns for (a, b) top and side views for $\alpha = 32$ deg, (c, d) top and side views for $\alpha = 44$ deg.

simulations are discussed with respect to the experimental results of Ref. 12.

Figures 3, 5b, 6b, 7, and 8b present the results for this case where $\alpha = 20$ deg and the flow is assumed to be fully turbulent. The turbulent boundary layers are substantially thicker with larger pressure recoveries ahead of the separation lines owing to the increased mixing in the turbulent layer (Fig. 7). The magnitude of C_f is larger everywhere except in the secondary vortex region for the turbulent case. The turbulent flow is more resistant to separation, consequently the secondary vortex is much weaker. The primary separation at Station II occurs around $\eta = 90$ deg through a strong crossflow shock, with its core closer to the body than the laminar case (Figs. 6 and 7). The secondary separation and reattachment are around $\eta = 31$ deg and $\eta = 51$ deg, respectively. The longitudinal growth of the leeside vortex sheets is substantially delayed, as it can be observed through a comparison of the skin friction patterns for the laminar and the turbulent cases (Fig. 8). The primary vortex at Station I for the laminar case (Fig. 5a) has disappeared for the turbulent case (Fig. 5b).

Laminar Flow at $\alpha = 32$ Deg

Since the flow over a body of $L/D = 6.67$ at $\alpha \geq 32$ deg has the potential to develop asymmetrically (Fig. 1), the full-body grid was used for this case. Although the flows at $Re_D = 5 \times 10^5$ over an ogive cylinder at $\alpha = 32$ deg and $\alpha = 44$ deg may develop transitional boundary layers,[6] they were assumed laminar in this study. Figure 9 shows the agreement between the computed and measured[12] longitudinal C_p distributions on the body at fixed circumferential locations. The computational and experimental values for C_N were 4.11 and 4.19, respectively. A comparison of crossflow density contours at Stations I and II (Fig. 10) demonstrates the growth of both the leeside vortex sheets as the distance increases from the nose as well as the cross section of the shock surface on the windside. The skin friction patterns (Fig. 11a) show that the convergence lines begin closer to the nose for this case than the $\alpha = 20$ deg case. That is, the separation occurs nearer to the nose for larger angles of attack, as it was also observed in Ref.

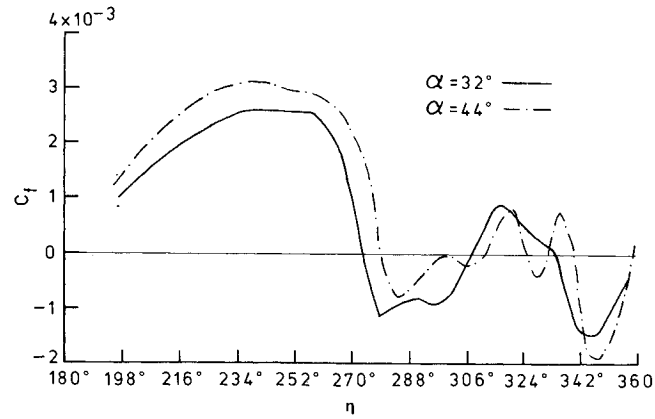

Fig. 12 Circumferential skin friction distribution at Station II for $\alpha = 32$ deg and $\alpha = 44$ deg.

4. Figure 12 shows the circumferential C_f distribution of the body at Station II. The primary separation occurs around $\eta = 274$ deg (86 deg) and the primary reattachment fluctuates about $\eta = 360$ deg for ± 3 deg. The secondary separation and reattachment are computed to be around $\eta = 335$ deg (25 deg) and $\eta = 308$ deg (52 deg), respectively.

Laminar Flow at $\alpha = 44$ Deg

The comparison of computed and experimental longitudinal surface C_p distributions, and the comparison of density contours of the symmetry plane with its Schlieren photograph, are shown in Figs. 8 and 13, respectively. The computed value of C_N (6.15) was within 4% of its experimental value (6.38). Convergence of the skin friction patterns (Fig. 11b) is closer to the nose longitudinally, and to the leeside circumferentially, than $\alpha = 20$ deg and $\alpha = 32$ deg cases. The circumferential C_f distribution at Station II (Fig. 12) shows the primary separation to be around $\eta = 279$ deg (81 deg). The mild asymmetry of the crossflow about $\eta = 0$ deg plane starts with the primary reattachment (Figs. 11b and 14). The secondary separation

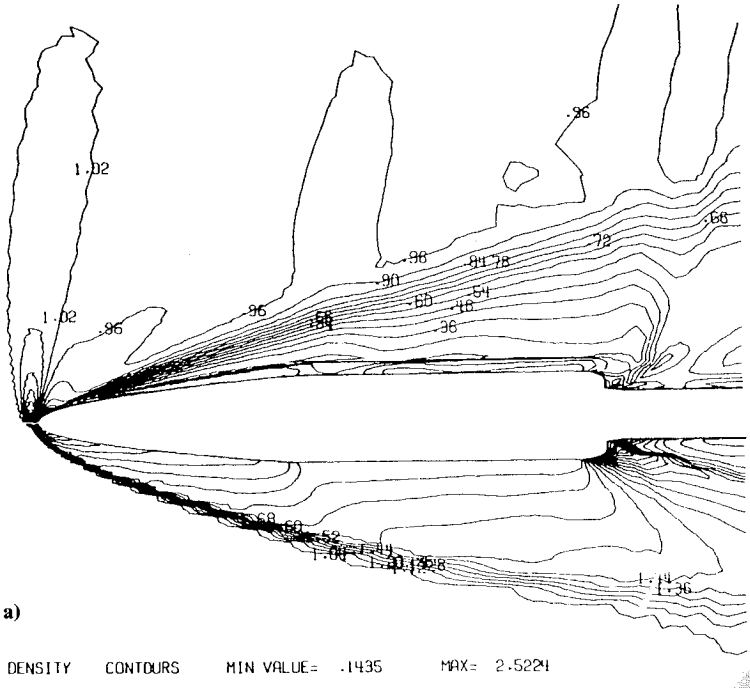

a)

DENSITY CONTOURS MIN VALUE= .1435 MAX= 2.5224

b)

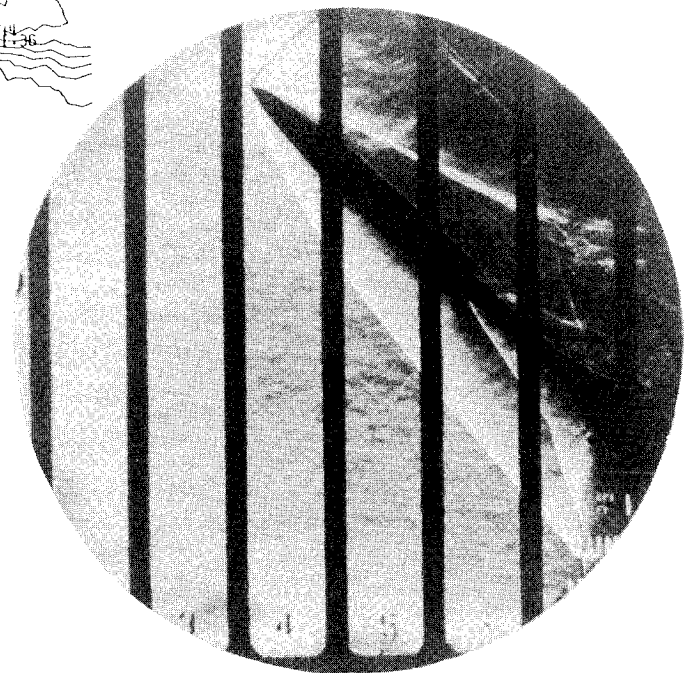

Fig. 13 a) Normalized density contours; and b) Schlieren photograph[12] of the symmetry plane for $\alpha = 44$ deg.

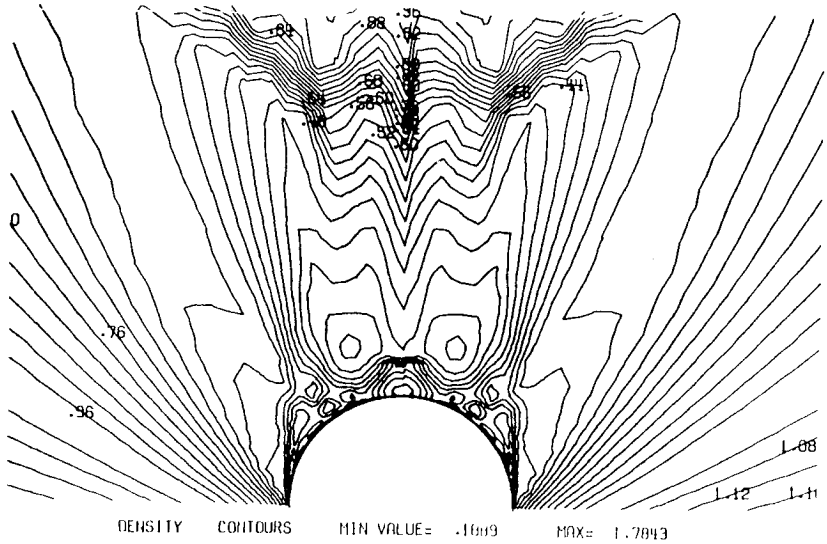

DENSITY CONTOURS MIN VALUE= .1019 MAX= 1.7843

Fig. 14 Normalized crossflow density contours at Station II for $\alpha = 44$ deg.

and reattachment at Station II occur around $\eta = 338$ deg (22 deg) and $\eta = 312$ deg (48 deg), respectively, inducing vortices that rotate in the opposite directions of the primary vortices.

Although reasons for an asymmetrical flow structure about a symmetrical body are not conclusively shown in the literature, two basic mechanisms are often given to describe this phenomenon: 1) formation of asymmetric vortex patterns in the wake of the body; and 2) asymmetry of the flow ahead of the primary separation lines because of different transitional states of the boundary layer occurring on either side of the cylinder, for example due to surface roughness. Since the mathematical formulation of this study accounts neither for the possible transitions from laminar to turbulence regimes nor for surface roughness effects, the latter mechanism could not be verified. Owing to the supersonic nature of the flow, it is less likely that the former mechanism would have any significant influence, because the effect of the wake could only be sensed through the subsonic regions embedded in the boundary layer. However, it was concluded that the major reason for the near-symmetric flow even at an angle of attack as high as 44 deg, was the bluntness of the forebody. The minor reasons were concluded to be the Reynolds number being critical (supercritical Reynolds number generates more asymmetry), and the moderate length to diameter ratio of the cylinder.

Conclusions

Vortical supersonic flows over a blunt-nose-cylinder at high angles of attack were computationally simulated. Solutions were obtained using techniques that were numerically and computationally very efficient. It was shown that with the increasing angle of attack, the separation and reattachment lines and subsequent vortex sheets moved toward the leeside, and the normal force coefficient increased. Although slight asymmetry was noticed off the body and around the primary reattachment point for $\alpha = 32$ deg and $\alpha = 44$ deg, the asymmetric vortex flow was largely avoided due to the blunt nose. It was observed that turbulence increased resistance of the flow to separation with larger pressure recoveries at separation lines resulting in crossflow shocks.

Acknowledgment

This work was supported under NASA Grant NAG-1-664.

References

[1]Degani, D. and Schiff, L. B., "Computation of Turbulent Supersonic Flows Around Pointed Bodies Having Crossflow Separation," *Journal of Computational Physics,* Vol. 66, Sept. 1986, pp. 173–196.

[2]Newsome, R. W., "Numerical Simulation of Vortical Flow Over an Elliptical-Body Missile at High Angles of Attack," AIAA Paper 86-0559, Jan. 1986.

[3]Hankey, W. L., Graham, J. E., and Shang, J. S., "Navier-Stokes Solution of a Slender Body of Revolution at Incidence," *AIAA Journal,* Vol. 20, June 1982, pp. 776–781.

[4]Yates, L. A. and Chapman, G. T., "A Numerical Investigation of Crossflow Separation on a Three-Caliber Ogive-Cylinder," AIAA Paper 87-1209, June 1987.

[5]Chapman, G. T. and Keener, E. R., "The Aerodynamics of Bodies of Revolution at Angles of Attack," AIAA Paper 79-0023, Jan. 1979.

[6]Lamont, P. J., "Pressure Around an Inclined Ogive Cylinder with Laminar, Transitional, or Turbulent Separation," *AIAA Journal,* Vol. 20, Nov. 1982, pp. 1482–1499.

[7]Baldwin, B. S. and Lomax, H., "Thin Layer Approximation and Algebraic Model for Separated Flows," AIAA Paper 78-257, Jan. 1978.

[8]Van Leer, B., Thomas, J. L., Roe, P. L., and Newsome, R. W., "A Comparison of Numerical Flux Formulas for Euler and Navier-Stokes Equations," AIAA Paper 87-1104-CP, June 1987.

[9]Thomas, J. L., Taylor, S. L., and Anderson, W. K., "Navier-Stokes Computations of Vortical Flows Over Low Aspect Ratio Wings," AIAA Paper 87-0207, Jan. 1987.

[10]Baysal. O., "Supercomputing Supersonic Flows Using Upwind Relaxation and MacCormack Schemes," *ASME Journal of Fluids Engineering,* Vol. 110, No. 1, March 1988, pp. 62–68.

[11]Vatsa, V. N., Thomas, J. L., and Wedan, B. W., "Navier-Stokes Computations of Prolate Spheroids at Angle of Attack," AIAA Paper 87-2627-CP, Aug. 1987.

[12]Landrum, E. J. and Babb, C. D., "Wind-Tunnel Force, Pressure and Flow Visualization Data at Mach Numbers from 1.6 to 4.63 for a Series of Bodies of Revolution at Angles of Attack from $-4°$ to 60°," NASA-TM-X-3558, Oct. 1977, and NASA-TM-78813, March 1979.